ELSEVIER

Magnetic Resonance Imaging 21 (2003) 1113-1120
Research articles

MAGNETIC RESONANCE IMAGING

# Magnetization transfer MRI of mouse brain reveals areas of high neural density

O. Natt*, T. Watanabe, S. Boretius, J. Frahm, T. Michaelis

*Biomedizinische NMR Forschungs GmbH am Max-Planck-Institut für biophysikalische Chemie, 37070 Göttingen, Germany*

Received 15 August 2003; received in revised form 22 August 2003; accepted 23 August 2003

**Abstract**

Extending applications of magnetization transfer contrast (MTC) in magnetic resonance imaging (MRI) of the human central nervous system, this work quantitatively describes MTC of the murine brain. As a novel finding, complementing $T_1$- and $T_2$-weighted MRI, MTC allows for the distinction of densely packed gray matter from normal gray and white matter. Examples include the Purkinje cell layer and the granular cell layer in the mouse cerebellum as well as the delineation of the CA3 subfield of the hippocampus relative to surrounding hippocampal gray matter and white matter tracts such as the hippocampal fimbria. Using a kainate lesion model, the CA3 hyperintensities in MTC and $T_1$-weighted MRI are assigned to the densely packed somata of pyramidal cells. 

*Keywords:* Magnetization transfer (MT); Mouse brain; Cerebellum; Hippocampus; CA3

## 1. Introduction

In vivo magnetic resonance imaging (MRI) of the mouse brain at high spatial resolution allows for the identification of a large number of cerebral microstructures and offers repeated studies of the same animal [1]. Despite the availability of excellent soft-tissue contrast in $T_1$- and $T_2$-weighted MRI, the physical nature of the underlying differences in nuclear magnetic relaxation times restricts the structural information to specific aspects of the molecular mobility of intra- and extracellular water (and lipid) protons. Complementary morphologic information may be obtained by magnetization transfer (MT) techniques. As first observed by Wolff and Balaban [2], MT contrast (MTC) in MRI is based on the indirect saturation of the pool of observable "liquid" water protons ($T_2 > 10$ ms) after selective off-resonance saturation of the pool of less mobile or "semi-solid" protons ($T_2 < 1$ ms) bound to macromolecular structures such as proteins or membranes. Assuming dipolar interactions, proton exchange, and water exchange between both pools, the MT effect is quantitatively well understood for both model systems like agar gel [3–5] and biologic tissues [6–8].

So far, a widespread range of applications has been proposed (for a review, see [9]) with a particular emphasis on soft-tissue suppression in MR angiography and a delineation of white matter lesions in diseases such as multiple sclerosis. In contrast, little effort has been made to evaluate the MTC information in small laboratory animals such as mice. The purpose of this study was 1) to quantify MT model parameters in mouse brain in vivo; 2) to optimize MRI parameters for MTC of mouse brain in vivo; and 3) to examine whether MTC provides tissue-specific contrast beyond $T_1$- or $T_2$-weighted MRI.

## 2. Materials and methods

### 2.1. Animals

All studies were performed in accordance with German animal protection laws and approved by the responsible governmental authority. Young adult C57BL/6 mice ($n = 3$, male) and NMRI mice ($n = 3$, female) underwent MRI examinations at 2.35 T using a MRBR 4.7/400 mm magnet (Magnex Scientific, Abingdon, England) equipped with BGA20 gradients (100 mT $m^{-1}$) and driven by a DBX system (Bruker Biospin, Ettlingen, Germany).

For in vivo MRI studies, animals were intubated and kept under halothane anesthesia (1.0–1.5% halothane in 70:30

* Corresponding author. Tel.: +49-551-201-1726; fax: +49-551-201-1307.
*E-mail address:* onatt@gwdg.de (O. Natt).

0730-725X/03/$ – see front matter 
doi:10.1016/j.mri.2003.08.012

$N_2O$:$O_2$). All animals were placed in a prone position with their heads firmly fixed in a purpose-built stereotactic device. Radiofrequency (RF) excitation and signal reception were accomplished with use of a Helmholtz coil ($\phi$ 100 mm) and an elliptical surface coil (20 mm anterior-posterior, 12 mm left-right), respectively. The rectal body temperature was maintained constant at 37 ± 1°C using heated water blankets.

To elucidate the nature of hippocampal MRI contrasts FVB/N mice ($n$ = 2, male, 9 weeks old) were treated with a kainic acid lesion model. This strain was chosen because its pyramidal cells in the hippocampal CA3 region are known to be more susceptible to kainic acid than the cells of C57BL/6 mice [10]. FVB/N mice received a single subcutaneous injection of kainic acid (30 mg/kg, pH 7.3) or placebo (saline). During a subsequent 3 h observation period for behavioral symptoms, the lesioned animal showed signs of epileptic activity, including staring, decreased motility, twitching, rearing, and falling. $T_1$-weighted 3 D RF-spoiled FLASH MRI ($\alpha$ = 30°, TR = 22 ms, TE = 8.2 ms, 32 acumulations, measuring time 72 min) at 100 × 100 × 500 $\mu m^3$ resolution was performed before administration of kainic acid or placebo as well as 4 days later. Immediately after the second MRI examination, animals were transcardially perfused with neutral phosphate-buffered formalin (10 %). Horizontal brain sections were cut at a thickness of 40 $\mu$m. Every third section was stained with cresyl violet to determine neuronal cell loss.

### 2.2. Theory

The theoretical approach used here is based on a simple two-pool model originally developed for continuous wave (CW) experiments [3,11,12]. For the liquid proton pool (pool $a$) a Lorentzian lineshape

$$T^a = \frac{\omega_1^2 T_2^a}{1 + (\Delta T_2^a)^2} \approx \frac{\omega_1^2}{\Delta^2 T_2^a} \tag{1}$$

is assumed, with $\Delta$ the angular frequency offset and $\omega_1 = \gamma B_1$ the angular nutation frequency, which corresponds to the amplitude $B_1$ of the RF irradiation. For the semisolid pool (pool $b$), a super-Lorentzian lineshape has been shown to yield an adequate description in biologic tissue [7,13]

$$T^b = \sqrt{2\pi}\omega_1^2 T_2^b \int_0^1 \frac{1}{|3u^2 - 1|} \cdot \exp\left(-2\left(\frac{\Delta T_2^b}{3u^2 - 1}\right)^2\right) du. \tag{2}$$

Both lineshapes are characterized by a respective spin-spin relaxation time $T_2^a$ and $T_2^b$ representative of the liquid and semisolid pool.

For CW irradiation, the two-pool model leads to an analytic expression for the steady-state longitudinal magnetization $M_z^a$ of the liquid pool

$$M_z^a = M_0^a \frac{R^b + T^b + M_0^a R_x + R^b \frac{M_0^b R_x}{R^a}}{\left(1 + \frac{M_0^b R_x}{R^a} + \frac{\omega_1^2}{\Delta^2}\frac{1}{R^a T_2^a}\right)(R^b + M_0^a R_x + T^b) - M_0^a R_x \frac{M_0^b R_x}{R^a}}. \tag{3}$$

The exchange rate between both pools is characterized by the rate constant $R_x$, and the relative pool sizes are denoted by $M_0^a$ and $M_0^b$. The spin-lattice relaxivities of the liquid and the semisolid pool are denoted by $R^a$ and $R^b$, respectively.

Although Eq. (3) is strictly valid only for MT experiments with CW irradiation of the semisolid pool, it can be taken as a good approximation for pulsed experiments if the excitation pulses are sufficiently soft and the ratio of the repetition time TR and the pulse duration $T_p$ is sufficiently small [14]. For pulsed experiments, the amplitude of the off-resonant RF irradiation is given in terms of a CW equivalent amplitude [14]

$$B_1^{CW} = \sqrt{\frac{1}{TR}\int_0^{T_p} |B_1(\tau)|^2 d\tau}, \tag{4}$$

where $B_1(t)$ and $T_p$ are the time-domain shape and duration of the MT pulse, respectively. As proposed by others [3,14], the CW amplitude $B_1^{CW}$ is specified in terms of the corresponding nutation frequency ($\gamma B_1^{CW}/2\pi$).

### 2.3. Quantitative MT determinations

Measurements of MT model parameters were based on a 2 D RF-spoiled FLASH sequence ($\alpha$ = 5°, TR = 30 ms, TE = 7.1 ms, FOV = 20 × 20 $mm^2$, matrix size = 128 × 128, slice thickness = 2 mm, 64 accumulations). Off-resonant RF irradiation was accomplished with use of Gaussian RF pulses (1 % cutoff level, 12 ms duration) applied once per TR of the imaging sequence.

In order to evaluate MT parameters in accordance with Eq. (3), four different powers for off-resonant RF irradiation (100, 200, 300, and 400 Hz corresponding to flip angles of 522, 1045, 1567, and 2090°) were combined with nine different frequency offsets ranging from 1 to 70 kHz in logarithmic steps (1000, 1701, 2893, 4919, 8367, 14229, 24201, 41159, and 70000 Hz). Additional acquisitions were performed without MT pulses. Each measurement was preceded by a 20 s period of dummy scans in order to drive the spin system into steady state. The total measurement time for an in vivo mouse examination was about 3 h.

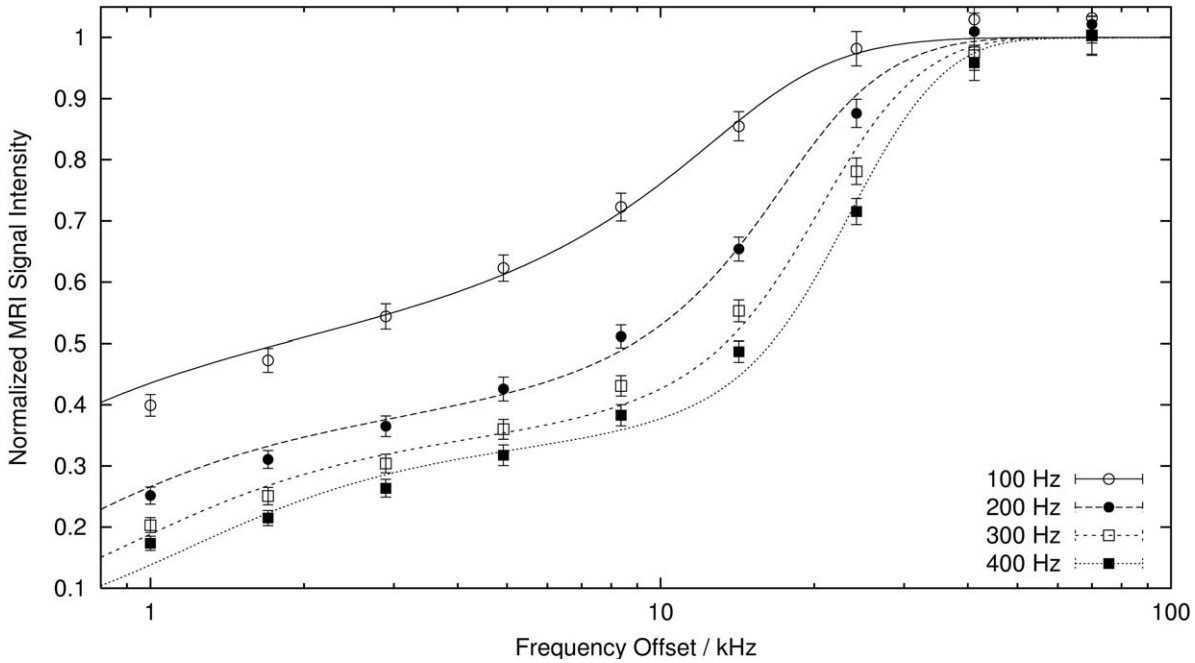


Fig. 1. Magnetization transfer in frontal gray matter of a C57BL/6 mouse in vivo. The normalized MRI signal intensity (mean ± SD of the region-of-interest) is plotted versus the frequency offset (logarithmic scale) for four different RF amplitudes. The lines represent fits of Eq. (3) to the data using a super-Lorentzian line shape for the pool of semi-solid protons.

### *2.4. Parameter estimation and optimization of MTC*

The MRI signal intensity for the MT measurements was determined in a gray matter (GM) region-of-interest of the frontal cortex as mean ± SD. All intensities were normalized by the mean of four measurements obtained without off-resonant RF irradiation. After normalization, the residual model parameters $R^b$, $T_2^b$, $M_0^b R_x/R^a$, $1/(R^a T_2^a)$, and $R_x$ were obtained by fitting the data to Eq. (3) by means of a least-squares algorithm. Because the model is largely insensitive to variations of $R_b$, this parameter was set to $R_b = 1$ s [3,8]. The errors for the model parameters were taken as the square roots of the diagonal elements of the covariance matrix.

Using Eq. (3) and a valid set of model parameters, the percentage saturation $S_{\text{total}}$ of the liquid pool resulting from the MT effect and the (unwanted) direct irradiation yields

$$S_{\text{total}} = 100 \cdot (1 - M_z^a). \tag{5}$$

The direct percentage saturation $S_{\text{direct}}$ is given by Eq. (3) when setting the exchange rate $R_x$ between both pools to zero.

$$S_{\text{direct}} = 100 \cdot (1 - \lim_{R_x \to 0} M_z^a). \tag{6}$$

The percentage saturation $S_{\text{MT}}$ of the liquid pool caused by MT should be maximized to achieve an optimum MTC. It is given by the difference of Eq. (5) and Eq. (6)

$$S_{\text{MT}} = S_{\text{total}} - S_{\text{direct}}. \tag{7}$$

### *2.5. High-resolution 3-D MRI*

In accordance with previous high-resolution $T_1$- and $T_2$-weighted MRI studies of mouse brain [1], all imaging protocols were based on a field-of-view of 15 × 15 × 15 mm and 3-D data acquisition matrices of 128 × 96 × 96. After interpolation to 128 × 128 × 128, the images had a resolution of 117 × 117 × 117 $\mu$m$^3$. The positions of horizontal or coronal sections were specified relative to the anterior commissure (AC).

$T_1$-weighted MRI employed a 3-D RF-spoiled FLASH sequence ($\alpha$ = 25°, TR = 30 ms, TE = 7.6 ms, 32 accumulations, measuring time 84 min). $T_2$ contrast was achieved with use of an efficient fast spin-echo (FSE) sequence (flip angles 90° and 180°, TR = 3 s, TE = 98 ms, 16 echoes, 2 accumulations, measuring time 58 min). For MT-weighted MRI, an off-resonant RF irradiation with a frequency offset of 5 kHz and a mean amplitude of 200 Hz (flip angle 1045°) was incorporated into a spin density-weighted 3-D FLASH sequence ($\alpha$ = 5°, TR = 30 ms, TE = 7.6 ms, 18 accumulations, measuring time 84 min).

## 3. Results and discussion

### *3.1. MT model parameters*

Fig. 1 shows the results obtained for quantitative MT measurements in the frontal GM of a C57BL/6 mouse in vivo. The fit of Eq. (3) to the experimental data ($\sigma$ = 0.021)

Table 1
MT model parameters for gray matter (GM) and white matter (WM)

| | $B_0$/T | $T_2^b$/μs | $M_0^b R_x / R^a$ | $1/(R^a T_2^a)$ | $R_x$/s$^{-1}$ |
|---|---|---|---|---|---|
| C57BL/6 GM | 2.35 | 9.3 ± 0.3 | 2.2 ± 0.1 | 26 ± 4 | 14 ± 2 |
| NMRI GM | 2.35 | 9.3 ± 0.3 | 2.3 ± 0.1 | 30 ± 3 | 17 ± 2 |
| NMRI GM[a] | 2.35 | 9.5 ± 0.4 | 2.0 ± 0.1 | 20 ± 2 | 21 ± 3 |
| Rat GM [6][b] | 4.7 | 8.5 ± 0.6 | 2.1 ± 0.1 | 100 ± 11 | 12 ± 2 |
| Rat WM [6][c] | 4.7 | 9.4 ± 0.8 | 2.8 ± 0.2 | 99 ± 17 | 16 ± 2 |
| Bovine GM [7][c] | 1.5 | 9.2 ± 0.4 | 1.7 ± 0.1 | 16 ± 2 | 32 ± 4 |
| Bovine WM [7][d] | 1.5 | 10.4 ± 0.5 | 2.0 ± 0.1 | 23 ± 4 | 21 ± 3 |
| Human GM [8] | 1.5 | 11.1 ± 1.3 | 2.6 ± 1.0 | 19 ± 5 | 33 ± 13 |
| Human WM [8] | 1.5 | 12.3 ± 1.6 | 2.4 ± 0.7 | 15 ± 4 | 27 ± 8 |

[a] Post mortem.
[b] Temporal lobe.
[c] In vitro.
[d] Corpus Callosum.

is excellent and within the range reported in a study on bovine samples in vitro [7], where $\sigma$ is defined by

$$\sigma = \sqrt{\frac{1}{N}\sum_{i=1}^{N}(\text{fit}_i - \text{data}_i)^2} \tag{8}$$

with $N$ the number of data points. Table 1 summarizes the determined model parameters for C57BL/6 and NMRI mice in vivo as well as for a NMRI mouse post mortem. The results are compared with corresponding values obtained for CW experiments of both rats in vivo [6] and samples of bovine GM and white matter (WM) in vitro [7] as well as for pulsed MT experiments in humans [8].

The model parameters obtained for mice are in general agreement with respective values reported for other species (rat, bovine, human) and at different field strengths (1.5 T, 2.35 T, 4.7 T). This particularly applies to $T_2^b$ of the semi-solid pool, which is on the order of 10 μs, and the exchange rate $R_x$, which ranges between 15 and 30 s$^{-1}$. The absence of a pronounced field strength dependence is in line with measurements of MT model parameters in agarose phantoms performed at 0.6 T and 1.5 T [3]. Moreover, the present findings suggest that the amount, structure, and dynamics of the brain's macromolecular content—at least as far as detectable by MT-weighted MRI—are rather similar in the species investigated.

### 3.2. Optimum imaging parameters for MTC

Fig. 2 shows the degree of MT-induced saturation $S_{MT}$ as obtained from Eq. (7) and the model parameters for C57BL/6 mice in vivo. A maximum MT effect with a saturation of 58.8 % requires a relatively high RF amplitude of 536 Hz and a frequency offset of 11.1 kHz. This result is in line with studies which either theoretically predicted an optimum MTC at very high RF amplitudes [14] or directly observed the MTC by MRI [6]. However, even much lower RF amplitudes on the order of 200 Hz can lead to a significant MT effect of more than 50% saturation, if the frequency offset is adapted to the RF amplitude. This optimization is indicated by a shaded line in Fig. 2.

### 3.3. Soft-tissue contrast

Fig. 3 compares high-resolution MR images of a mouse brain in vivo with MTC to corresponding acquisitions with $T_1$ and $T_2$ contrast. At first glance, visual inspection reveals a superficial resemblance of the MT-weighted image to the $T_2$-weighted image: in either case, the ventricular spaces present with hyperintensities and WM structures exhibit very low signal intensities. Using MTC, the cerebrospinal fluid (CSF) appears bright because of its low macromolecular content, whereas WM appears dark due to a pronounced saturation of mobile protons through interactions with the large pool of bound protons in bundles of myelinated axons. However, MTC provides additional information beyond the contrast capabilities of $T_1$- or $T_2$-weighted images, as it relies on a different physical principle. This complementary soft-tissue contrast becomes most prominent in the cerebellum and hippocampal formation.

Focusing on the mouse cerebellum, Fig. 4 again compares MTC with $T_1$ and $T_2$ contrast. It turns out that the gross appearance of $T_1$- and $T_2$-weighted images is dominated by the respective low and high signal intensities of CSF, partially obscuring other tissues such as GM and WM. For example, when using $T_2$ contrast, WM is barely visible as three dark bands. Conversely, MTC reveals a clear delineation of true WM structures because of their pronounced hypointensities. It is of note that the directly adjacent rims of tissue present with bright intensities. These structures

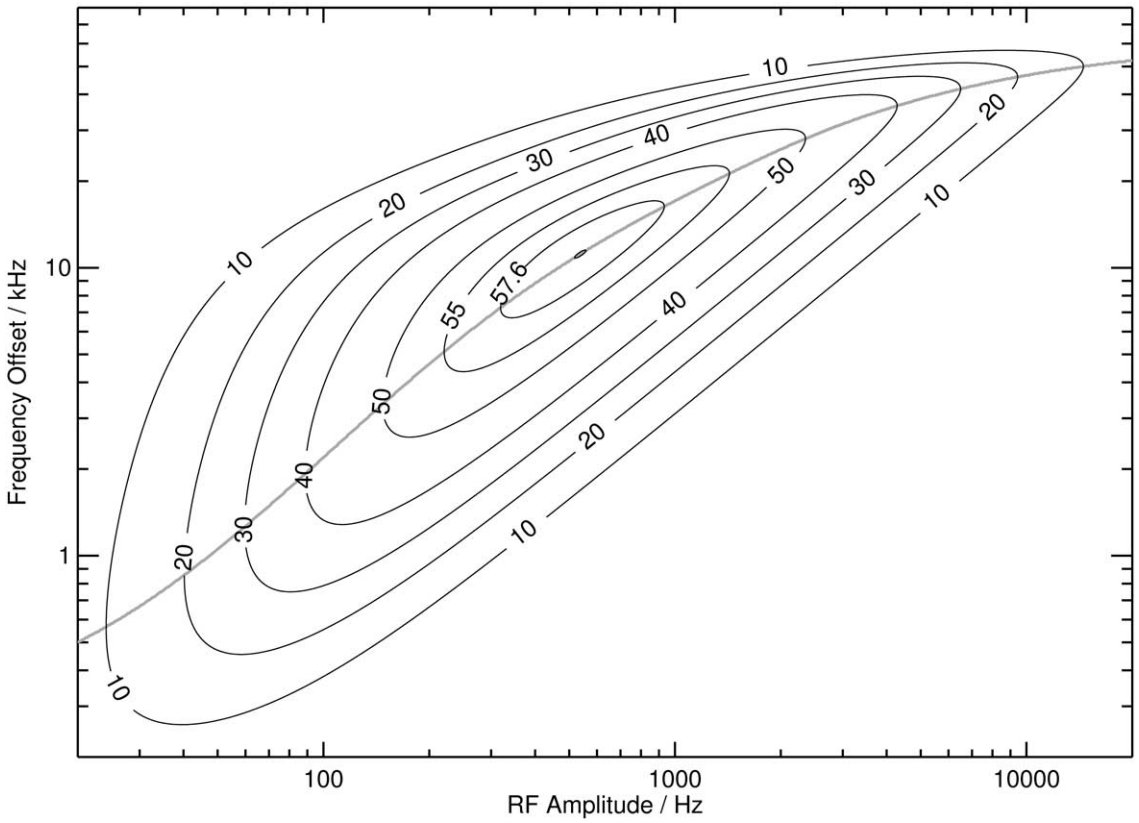


Fig. 2. The contours show the degree of MT saturation of the pool of liquid protons (in percent, without direct saturation) as determined by Eq. (7) using the parameters found for mouse brain in vivo (Table 1). Maximum saturation (58.8%) is achieved for an RF amplitude of 536 Hz and a frequency offset of 11.1 kHz. The shaded line indicates the optimum frequency offset for each RF amplitude.

most likely correspond to the glomerular layer and the layer of Purkinje cell bodies and are therefore best described as "densely packed" GM. Further contributions with slightly reduced intensities may arise from the molecular layer in agreement with histologic sections of mouse cerebellum (e.g., see [15,16]).

The above results indicate that MTC, which is based on differences in macromolecular content rather than in molecular mobility, allows for a differentiation of WM (dark) and densely packed GM (bright), whereas both structures appear isointense in either $T_1$-weighted MRI (bright) or $T_2$-weighted MRI (dark). This hypothesis is further supported by a comparison of respective contrasts in the mouse hippocampus shown in Fig. 5. While $T_1$- and $T_2$-weighted images depict the CA3 subfield of the hippocampus with similar signal intensity as the WM in the hippocampal fimbria or the external capsule, the MTC image clearly distincts the bright CA3 region from the hypointense WM.

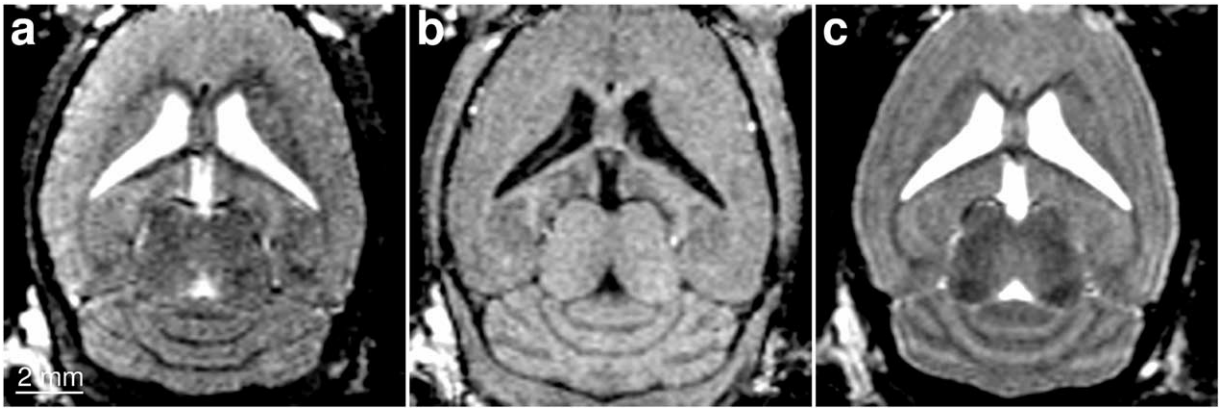


Fig. 3. MTC (3D FLASH) (a), $T_1$ contrast (3D FLASH) (b), and $T_2$ contrast (3D FSE) (c) of the brain of a C57BL/6 mouse in vivo in horizontal sections (3.0 mm dorsal to AC).

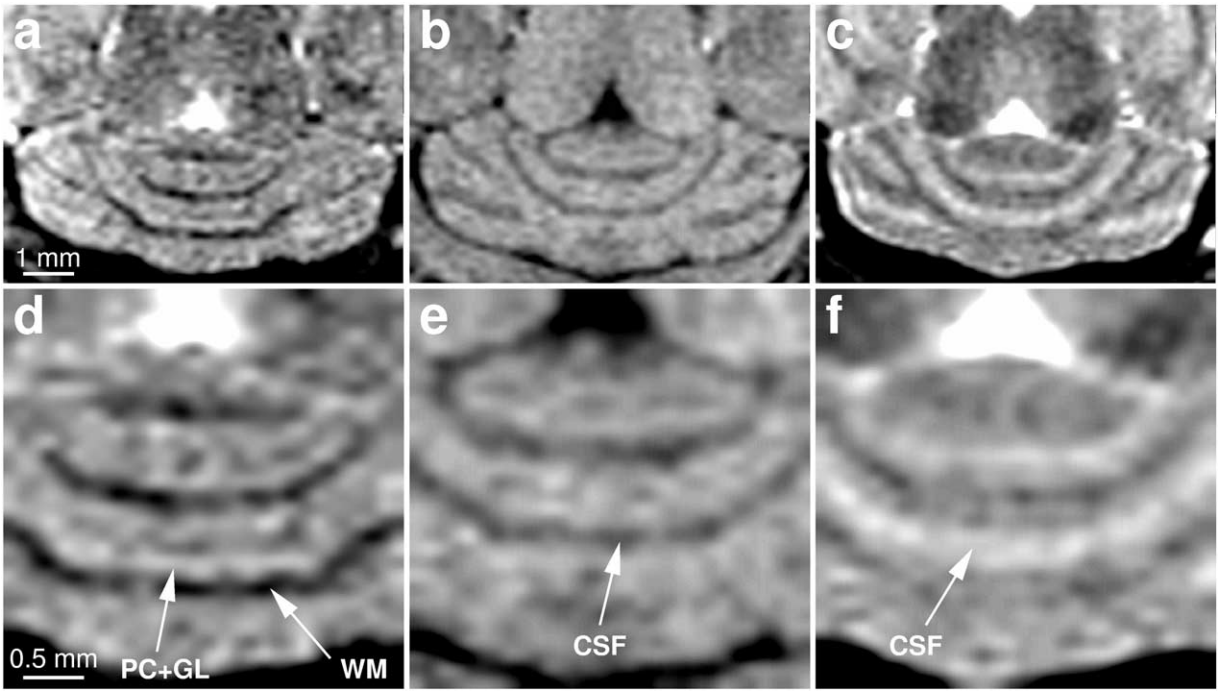


Fig. 4. MTC (a,d), $T_1$ contrast (b,e), and $T_2$ contrast (c,f), of the cerebellum of a mouse in vivo in (top) horizontal sections (3.0 mm dorsal to AC) and (bottom) corresponding magnified views. Apart from white matter (WM) hypointensities due to strong RF saturation, MTC reveals adjacent layers of bright signal which most likely reflect densely packed gray matter from the bodies of Purkinje cells (PC) and granular cells (GL). In contrast, $T_1$-and $T_2$-weighted images are dominated by low or high signal intensities from CSF, respectively.

Histologic sections of the mouse hippocampus (e.g., see [17,18]) suggest the layer of pyramidal cell bodies to be largely responsible for the bright MTC appearance of the CA3 region. This assumption is strongly supported by the results shown in Fig. 6 which compare $T_1$-weighted images and corresponding histologic sections of a placebo-treated mouse and a lesioned animal 4 days after administration of kainate. In line with the fact that this well established model of neuronal cell death in CA3 [19] primarily targets pyramidal cells (layer thickness about 100–120 $\mu$m), the histologic staining reveals a marked loss of cell bodies in CA3 of the affected animal. The corresponding loss of MRI signal intensity therefore supports the assignment of the bright $T_1$ contrast to the presence of viable pyramidal cells. As a consequence, the bright MTC of the CA3 subfield in Fig. 5, which further eliminates putative contributions from the axonal fibers, must be ascribed to the densely packed layer of pyramidal cell bodies.

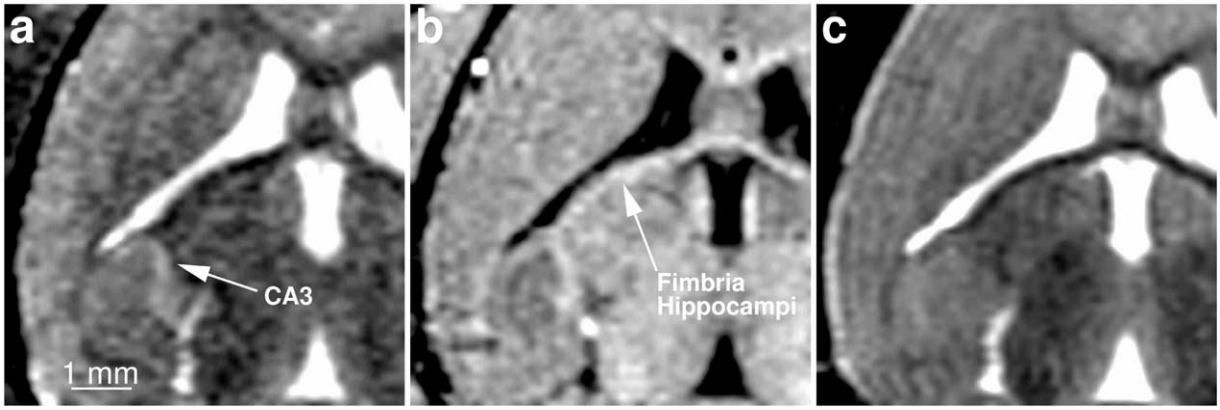


Fig. 5. MTC (a), $T_1$ contrast (b), and $T_2$ contrast (c) of the right hippocampus of a mouse in vivo (horizontal sections 2.7 mm dorsal to AC). Whereas MTC reveals a bright signal in the CA3 subfield, which refers to a high neural density of pyramidal cells, $T_1$-weighted MRI highlights white matter in both the hippocampal fimbria and CA3 region. In $T_2$-weighted MRI, CA3 appears isointense with adjacent areas.

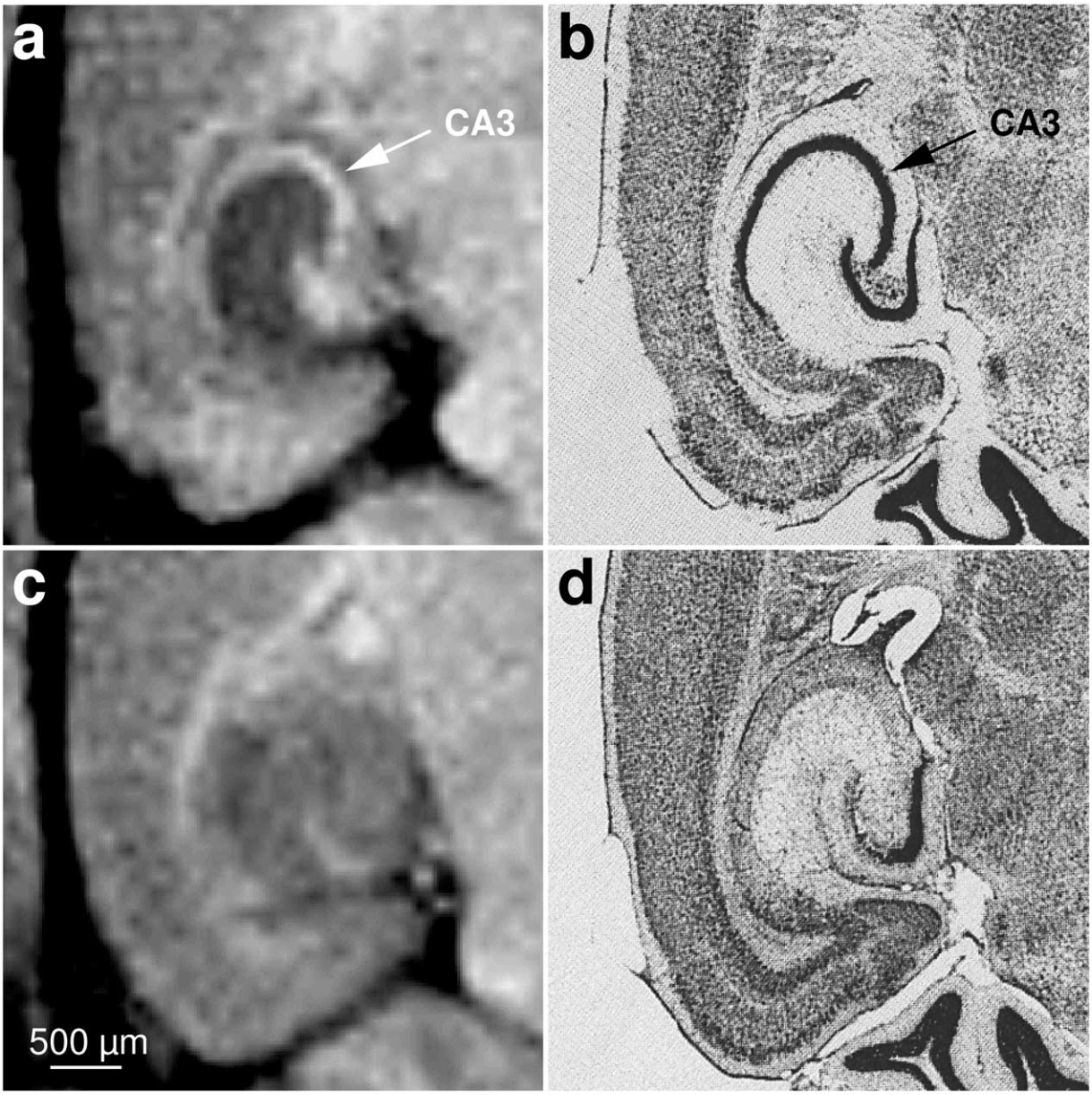


Fig. 6. $T_1$-weighted MRI in vivo (horizontal sections 1.0 mm dorsal to AC) (a,c) and histology (cresyl violet staining for neuronal cells) of the right hippocampus (b,d) of a placebo-treated FVB/N mouse (top) and a mouse 4 days after administration of kainic acid (bottom). The lack of pyramidal cells in the CA3 subfield of the lesioned animal (dark area in the histologic section) corresponds to the loss of $T_1$-weighted MRI signal intensity.

## 4. Conclusions

Extending the use of MTC in studies of the human central nervous system, this work provides MTC-based morphologic information of murine brain, which is otherwise not accessible by conventional $T_1$- or $T_2$-weighted MRI. The novel finding that MTC allows a distinction of densely packed GM from WM renders MT-weighted MRI particularly interesting for investigations of the cerebellum and hippocampal formation in mouse models of respective brain disorders. Further studies that attempt to exploit this possibility in humans are in progress.

## Acknowledgments

The authors would like to thank Stefanie Gleisberg (German Primate Center) for the preparation of histological sections.

## References

[1] Natt O, Watanabe T, Boretius S, Radulovic J, Frahm J, Michaelis T. High-resolution 3D MRI of mouse brain reveals small cerebal structures in vivo. J Neurosci Meth 2002;120:203–9.

[2] Wolff SD, Balaban RS. Magnetization transfer contrast (MTC) and tissue water proton relaxation in vivo. Magn Reson Med 1989;10: 135–44.
[3] Henkelman RM, Huang X, Xiang QS, Stanisz GJ, Swanson SD. Quantitative interpretation of magnetization transfer. Magn Reson Med 1993;29:759–66.
[4] Pike GB. Pulsed magnetization transfer contrast in gradient echo imaging: a two-pool analytic description of signal response. Magn Reson Med 1996;36:95–103.
[5] Sled JG, Pike GB. Quantitative interpretation of magnetization transfer in spoiled gradient echo MRI sequences. J Magn Reson 2000; 145:24–36.
[6] Quesson B, Thiaudière E, Delalande C, Dousset V, Chateil JF, Canioni P. Magnetization transfer imaging in vivo of the rat brain at 4.7 T: interpretation using a binary spin-bath model with a superlorentzian lineshape. Magn Reson Med 1997;38:974–80.
[7] Morrison C, Henkelman RM. A model for magnetization transfer in tissues. Magn Reson Med 1995;33:475–482 (Erratum: Magn Reson Med 1966;35:277.).
[8] Sled JG, Pike GB. Quantitative imaging of magnetization transfer exchange and relaxation properties in vivo using MRI. Magn Reson Med 2001;46:923–31.
[9] Henkelmann RM, Stanisz GJ, Graham SJ. Magnetization transfer in MRI: a review. NMR Biomed 2001;14:57–64.
[10] Schauwecker PE, Steward O. Genetic determinants of susceptibility to excitotoxic cell death: implications for gene targeting approaches. Proc Natl Acad Sci USA 1997;94:4103–108.
[11] Wu X. Lineshape of magnetization transfer via cross relaxation. J Magn Reson 1991;94:186–90.
[12] Caines GH, Schleich T, Rydzewski JM. Incorporation of magnetization transfer into the formalism for rotating-frame spin-lattice proton NMR relaxation in the presence of an off-resonance-irradiation field. J Magn Reson 1991;58:558–66.
[13] Morrison C, Stanisz G, Henkelman RM. Modeling magnetization transfer for biological-like systems using a semi-solid pool with a super-lorentzian lineshape and dipolar reservoir. J Magn Reson B 1995;108:103–13.
[14] Hua J, Hurst GC. Analysis of on- and off-resonance magnetization transfer techniques. J Magn Reson Imaging 1995;5:113–20.
[15] Yamada K, Fukaya M, Shibata T, Kurihara H, Tanaka K, Inoue Y, Watanbe M. Dynamic transformation of Bergmann glial fibers proceeds in correlation with dentritic outgrowth and synapse formation of cerebellar Purkinje cells. J Comp Neurol 2000;418:106–20.
[16] Ozol K, Hayden JM, Oberdick J, Hawkes R. Transverse zones in the vermis of the mouse cerebellum. J Comp Neurol 1999;412:95–111.
[17] Jinno S, Aika Y, Fukuda T, Kosaka T. Quantitative analysis of GABAergic neurons in mouse hippocampus with optical disector using confocal laser scanning microscopy. Brain Res 1998;814:55–70.
[18] Watanabe T, Natt O, Boretius S, Frahm J, Michaelis T. In vivo 3D MRI staining of mouse brain after subcutaneous application of $MnCl_2$. Magn Reson Med 2002;48:852–59.
[19] Ben-Ari Y, Cossart R. Kainate, a double agent that generates seizures: two decates of progress. Trends Neurosci 2000;23:580–87.